

On the Magnetic Field Extraction for On-Chip Inductance Calculation

A. Nentchev and S. Selberherr

Institute for Microelectronics, TU Wien, 1040 Vienna, Austria
{nentchev|selberherr}@iue.tuwien.ac.at

Abstract

The small dimensions of the on-chip interconnect structures provide the interesting opportunity of using the optimized model of dominant magnetic field even at very high operating frequencies for inductance and resistance extraction. The parameters are obtained from the field energy calculated from the magnetic field distribution in the simulation domain. Vector and scalar shape functions are used for finite element equation system assembling. Series of simulations for an on-chip spiral inductor at frequencies between 1 MHz and 100 GHz are performed to extract the parameters and to visualize the field distributions in the simulation area.

1 Introduction

High frequencies in an integrated circuit (IC) affect both, the resistance and the inductance of the on-chip interconnects [1, 2]. These often as parasitics treated parameters cause longer signal rise, fall, and delay times and limit the maximum allowed frequency of modern ICs. However, as the operating frequencies increase, small inductors of high speed circuits can be also actively used. They can be even constructed on the chip. Thus the inductance of an on-chip interconnect line can be a disadvantage or very useful depending on the application. Of course the collateral resistance must also be considered.

2 The Theoretical Background

The Maxwell equations for the dominant magnetic field (DMF) and time independent μ are given [3] by the expressions

$$\vec{\nabla} \times \vec{E} = -\mu \partial_t \vec{H}, \quad \vec{\nabla} \cdot (\mu \vec{H}) = 0, \quad \rho (\vec{\nabla} \times \vec{H}) = \vec{E}. \quad (1)$$

\vec{E} is the electric field intensity, \vec{H} is the magnetic field intensity, μ is the material's permeability, and ρ is the material's electric resistivity. The derivative with respect to time is shortly notated as ∂_t instead of $\partial/\partial t$. Applying the rotor operator to the third equation of (1) and substituting its right hand side by the first equation of (1) yields the following second-order differential equation

$$\vec{\nabla} \times (\rho \vec{\nabla} \times \vec{H}) + \mu \partial_t \vec{H} = 0. \quad (2)$$

For the stationary case ($\partial_t \vec{H} = 0$) the finite element analysis of (2) leads to an over-determined linear equation system [4]. The matrix of this system is positive semi-definite and its zero eigenvalues correspond to the number of tree edges in the graph spanned by the finite element mesh edges [5]. Since $\vec{\nabla} \times \vec{\nabla} \varphi = 0$, (2) may be written as

$$\vec{\nabla} \times (\rho \vec{\nabla} \times \vec{H}_1) + \mu \partial_t (\vec{H}_1 - \vec{\nabla} \varphi) = 0, \quad (3)$$

where $\vec{H}_1 = \vec{H} + \vec{\nabla} \varphi$, φ is an arbitrary scalar field and $\vec{\nabla} \varphi$ must exist. Equation (3) contains two unknown functions – the vector field \vec{H}_1 and the scalar field φ . Thus an additional independent criterion is needed. For numerically stable and unique calculation of \vec{H} it is natural to impose the divergence condition given by the second equation of (1), which has not been used till now

$$\vec{\nabla} \cdot [\mu (\vec{H}_1 - \vec{\nabla} \varphi)] = 0. \quad (4)$$

Thus the unknown fields \vec{H}_1 and φ are the solution of the partial differential equation system consisting of (3) and (4), which is a boundary value problem numerically calculated by FEM in a simulation domain \mathcal{V} enclosing the investigated structures. \vec{H}_1 is approximated by vector (edge) functions and φ by scalar functions

$$\vec{H}_1 = \sum_{j=1}^n c_j \vec{N}_j + \sum_{j=m+1}^k c_j \vec{N}_j, \quad \varphi = \sum_{j=n+1}^m c_j \lambda_j + \sum_{j=k+1}^l c_j \lambda_j.$$

Due to the FEM domain discretization the region of interest \mathcal{V} and its surface $\partial \mathcal{V}$ are subdivided into smaller mesh elements – tetrahedrons and triangles consisting of edge connected nodes. The boundary of the simulation area $\partial \mathcal{V}$ is divided into a Dirichlet boundary $\partial \mathcal{V}_{D1}$ and a Neumann boundary $\partial \mathcal{V}_{N1}$ for \vec{H}_1 and into a Dirichlet boundary $\partial \mathcal{V}_{D2}$ and a Neumann boundary $\partial \mathcal{V}_{N2}$ for φ , respectively ($\partial \mathcal{V} = \partial \mathcal{V}_{D1} + \partial \mathcal{V}_{N1}$ and $\partial \mathcal{V} = \partial \mathcal{V}_{D2} + \partial \mathcal{V}_{N2}$). The edges and the nodes in the simulation area are labeled with a set of integers. The non-Dirichlet edges are indexed from 1 to n and the non-Dirichlet nodes are indexed from $n+1$ to m ($m > n$). The non-Dirichlet edges are the edges which do not belong to $\partial \mathcal{V}_{D1}$, and the non-Dirichlet nodes are the nodes which do not belong to $\partial \mathcal{V}_{D2}$, respectively. The Dirichlet edges are labeled with integers from $m+1$ to k ($k > m$) and the Dirichlet nodes are labeled with numbers from $k+1$ to l ($l > k$), respectively. In a single mesh element \vec{N}_j the Whitney 1-Form vector basis function [6] is associated with the j -th edge and λ_j is the Lagrange interpolation polynomial at vertex j . Equation (3) is weighted by the vector functions \vec{N}_i associated with the non-Dirichlet edges ($i \in [1; n]$) and (4) is weighted by the scalar functions λ_i associated with the non-Dirichlet nodes ($i \in [n+1; m]$) of the simulation domain. The inductance and the resistance are calculated by the magnetic energy and by the electric power, respectively

$$L = \frac{1}{I^2} \int_{\mathcal{V}} \mu H^2 dV, \quad R = \frac{1}{I^2} \int_{\mathcal{V}} (\vec{\nabla} \times \vec{H}_1) \cdot (\rho \vec{\nabla} \times \vec{H}_1) dV.$$

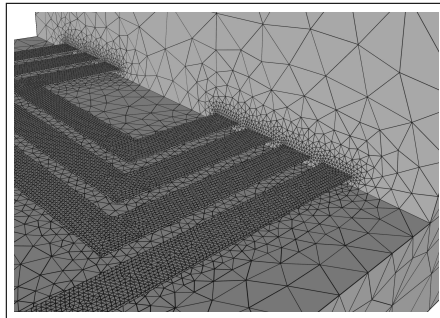
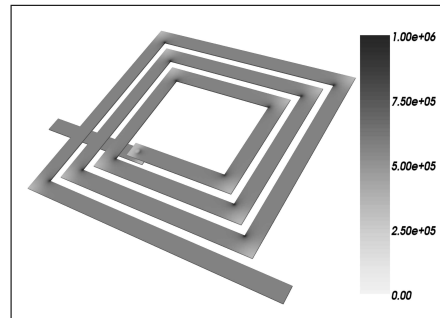
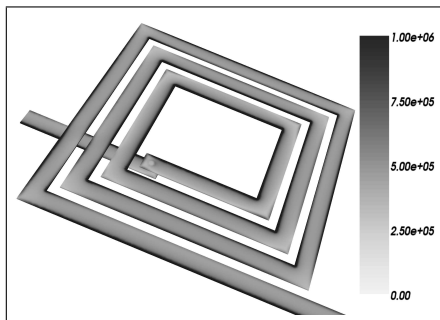
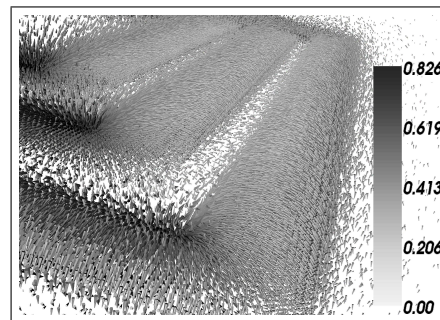
I is the total current in the inductor provided by the Dirichlet boundary for \vec{H}_1 .

$f [GHz]$	$L [nH]$	$R [\Omega]$
1	2.6516	3.463
10	2.5501	5.396
100	2.5458	13.156

Table 1: The inductance and resistance at different frequencies

3 Examples and Results

As example a typical on-chip spiral inductor structure is investigated. The inductor is placed in an insulating rectangular brick with dimensions $400 \mu m \times 400 \mu m \times 200 \mu m$. The cross-section of the conductor is $20 \mu m \times 1.2 \mu m$. The horizontal distance between the winding wires is $10 \mu m$. The outer dimensions of the inductor are $300 \mu m \times 300 \mu m$. The inductor is completely surrounded by the dielectric environment, except of the two small delimiting faces which lie directly in the boundary planes of the simulation domain. The conductor area and the dielectric area close to the conductor are discretized much finer than the remaining simulation domain. This is shown in Fig. 1 where a part of the dielectric environment is removed to visualize in detail the generated mesh inside the simulation domain. The variation of the fields in the finer discretized areas is expected to be much higher than in the coarser discretized domain. This special discretization reduces the number of generated nodes and edges, and the number of the linear equations respectively, even for big simulation environments which have to be used to satisfy the assumption of the homogeneous Neumann boundary condition. Of course such a discretization is only possible, if an unstructured mesh is used. The current density distribution depends heavily on the operating frequency in the analyzed frequency domain. It is unknown and a result of the simulation. At the beginning of the simulation only the total current in the inductor is known. The resistance and inductance values of the structure of interest are calculated numerically at different frequencies. The corresponding results are presented in Table 1. While the inductance decreases slowly with increasing operating frequency, the resistance rises dramatically, which matches well the observed current density distribution and the skin effect, respectively. A surface view of the current density distribution in the conductor is shown in Fig. 2 and Fig. 3 for 100MHz and 10GHz, respectively. At 100MHz the skin depth is about $6 \mu m$ and nearly the whole conductor cross-section is filled up by the current. At 10GHz the skin depth is about $0.6 \mu m$ and the current is concentrated at the vertical side walls of the conductor. Fig. 4 depicts the corresponding spatial distribution of the magnetic field inside the dielectric environment around the inductor as directed cones placed in the discretization nodes. The cones' size and darkness are proportional to the field strength. As the Q-factor of an inductor is inversely proportional to its resistance, making the inductor wire thicker might decrease the resistance and increase the Q-factor. However, as the examples show this is not the case for high frequencies at which the skin effect is noticeable. In these cases the current flows only in the area very close to the vertical surface and a wider transversal conductor cross section would not change the situation. For the visualization VTK [7] is used.

**Figure 1:** The generated mesh.**Figure 2:** Surface view of the current density $[A/m^2]$ distribution at 100 MHz.**Figure 3:** Surface view of the current density $[A/m^2]$ distribution at 10 GHz.**Figure 4:** Magnetic field intensity $[A/m]$ at 1 GHz.

References

- [1] Y. Cao, X. Huang, D. Sylvester, T.-J. King, and C. Hu. Impact of on-chip interconnect frequency-dependent $R(f)L(f)$ on digital and RF design. In *Proc. IEEE International ASIC-SoC Conference*, September 2002.
- [2] A. Nieuwoudt and Y. Massoud. Variability-aware multilevel integrated spiral inductor synthesis. *IEEE Trans. Comput.-Aided Design Integr. Circuits Syst.*, 25(12):2613–2625, December 2006.
- [3] A. Precht. Vorlesungen über Theoretische Elektrotechnik. Institut für Grundlagen und Theorie der Elektrotechnik, TU Wien, 1996. Zweiter Teil: Elektrodynamik.
- [4] P. Meuris, W. Schoenmaker, and W. Magnus. Strategy for electromagnetic interconnect modeling. *IEEE Trans. Comput.-Aided Design Integr. Circuits Syst.*, 20(6):753–762, June 2001.
- [5] O. Biró, K. Preis, and K. R. Richter. On the use of the magnetic vector potential in the nodal and edge finite element analysis of 3D magnetostatic problems. *IEEE Trans. Magn.*, 32(3):651–654, May 1996.
- [6] A. Bossavit. Whitney forms: A class of finite elements for three-dimensional computations in electromagnetism. *IEE Proceedings*, vol. 135, pp. 493–500, November 1988.
- [7] W. Schroeder, K. Martin, and B. Lorensen. *The Visualization Toolkit*. Kitware, Inc., USA, 2004.